Masteroppgave

NTNU
Norges teknisk-naturvitenskapelige universitet
Fakultet for ingeniørvitenskap
Institutt for konstruksjonsteknikk

Aleksander Jacobsen

1-Dimensional Modeling of Cerebrospinal Fluid Flow in Penetrating Arteriole Perivascular Spaces

Masteroppgave i MTPROD
Veileder: Prof. Leif Rune Hellevik
Medveileder: Prof. Kent-Andre Mardal

Januar 2024

NTNU
Kunnskap for en bedre verden

Aleksander Jacobsen

1-Dimensional Modeling of Cerebrospinal Fluid Flow in Penetrating Arteriole Perivascular Spaces

Masteroppgave i MTPROD
Veileder: Prof. Leif Rune Hellevik
Medveileder: Prof. Kent-Andre Mardal
Januar 2024

Norges teknisk-naturvitenskapelige universitet
Fakultet for ingeniørvitenskap
Institutt for konstruksjonsteknikk

NTNU
Kunnskap for en bedre verden

ABSTRACT

The clearance of waste products from the brain is crucial to brain health. Understanding the flow of cerebrospinal fluid through the perivascular spaces surrounding the brain vasculature is important for the prevention and treatment of disease, and due to the difficulties of physical flow and pressure measurements in the brain, numerical models are needed. As 3-dimensional fluid simulations are too computationally expensive, developing reliable, simplified models is a focus of research in this area. In this project, I derived and coded a 1-dimensional model that simulated CSF flow resulting from arterial pulsation in the penetrating arteriole PVS of a mouse and a human, respectively. To achieve this, I adapted an approach commonly used for simulating cardiovascular flow in arterial trees. By integrating the incompressible Navier Stokes equations over a cylindrical, annular control volume, I arrived at a set of 1-dimensional partial differential equations that I solved using a MacCormack scheme. The arterial pulsation was modeled as a sinusoidal radial movement applied uniformly on the inner wall, with an amplitude of 2.5% of the initial radius, and frequencies $f = [0.1, 1, 3, 10]$. The frequencies represent functional hyperemia, human heart rate during rest and exercise, and murine heart rate respectively.

Using this model, I was able to simulate oscillating flow with similar characteristics as those described in literature. There was however a considerable deviation in the results at the inlet and outlet, causing flows ranging from 1.34 to 3.23 times that of the internal nodes. This flow was shown to be unphysical as the flow rate heavily outweighed the rate of volume change. The average pressure gradient along the PVS was 12.5 Pa/mm and 2.5 Pa/mm for murine and human dimensions respectively, which is in the same order as in other simulations. The maximal Reynold's numbers in the trials ranged from $1.2{\times}10^{-2}$ to $3{\times}10^{-1}$ which is one to two orders of magnitude higher than the upper range of Reynold's numbers observed for similar systems.

In conclusion, the model presented was successful in simulating the expected pulsatile flow characteristics, with physiologically reasonable pressure gradient. However, the flow rate magnitude was too high, especially around the inlet boundary, where it was also unphysical.

SAMMENDRAG

Fjerning av avfallsprodukter fra hjernen er avgjørende for hjernehelse. En forståelse av flyten av cerebrospinalvæske i det perivaskulære rommet rundt hjernevaskulaturen er viktig for å forebygge og bekjempe sykdom, og på grunn av utfordringene ved å gjøre flyt- og trykkmålinger i hjernen, er det behov for numeriske modeller. Siden 3-dimensjonale flytsimuleringer er for kostbare med tanke på datakraft, er det et fokus i forskningen på å utvikle pålitelige, forenklede modeller. I dette prosjektet utledet og kodet jeg en 1-dimensjonal modell som simulerte cerebrospinalvæske-flyt i det perivaskulære rommet rundt en penetrerende arteriol for mus og menneske, som resultat av pulsering åreveggen. For å oppnå dette tilpasset jeg vanlig tilnærming brukt for å simulere kardiovaskulær flyt i blodåresystem. Ved å integrere de inkompressible Navier-Stokes-ligningene over et sylindrisk, ringformet kontrollvolum, kom jeg frem til et sett med 1-dimensjonale partielle differensialligninger som jeg deretter løste ved hjelp av et MacCormack-skjema. Arteriepulseringen ble modellert som en sinusformet radiell bevegelse påført uniformt på innerveggen, med amplitude 2,5% av startradiusen og med frekvenser $f = [0,1,1,3,10]$. Frekvensene representerer henholdsvis funksjonell hyperemi, menneskelig hjerteslag ved ro og trening, og hjerteslag hos mus.

Ved hjelp av denne modellen simulerte jeg oscillerende flyt med lignende flytkarakteristikker som er beskrevet i litteraturen. Det var derimot betydelige avvik i løsningen ved innløp og utløp som forårsaket strømningshastigheter opp til 1,34 ganger høyere enn ved interne punkter for menneskeforsøkene og 3,23 ganger høyere for museforsøkene. Denne flyten ble vist å være ufysisk da den utveide volumforandringen kraftig. Gjennomsnittlig trykkgradient langs det perivaskulære rommet var henholdsvis $12,5 Pa/mm$ og $2,5 Pa/mm$ for mus og menneskelig dimensjoner, som er i samme størrelsesorden som andre simuleringer. De maksimale Reynoldstallene i forsøkene varierte fra $1{,}2\times10^{-2}$ til 3×10^{-1}, som er en til to størrelsesordener høyere enn det øvre sjiktet funnet i liknende systemer.

For å oppsummere lyktes modellen å simulere realistiske pulserende flytkarakteristikker med fysiologisk rimelig trykkgradient. Flythastigheten var derimot for høy, spesielt rundt innløp og utløp, hvor den også var ufysisk.

PREFACE

This thesis is the conclusion of my Master's education at the Mechanical Engineering program at the Norwegian University of Science and Technology. When entering this program, I never imagined it would lead to writing a thesis related to medical science, but after attending a few lessons of Leif Rune's Biomechanics course, I realized this was what I wanted to specialize in. My fascination for the deeply challenging, yet even more interesting, field of computational biomechanics has only grown.

The thesis was written under the supervision of Professor Leif Rune Hellevik, at the Department of Structural Engineering, Norwegian University of Science and Technology (NTNU), and Professor Kent-Andre Mardal at the Department of Mathematics, University of Oslo (UiO). I would like to thank Leif Rune for the help during my thesis, and for initially introducing me to the field of Biomechanics. I would also like to thank Kent-Andre for all the help and guidance, and for giving me the opportunity to work in this exciting field. I want to thank Bjørg Næss Frost for being a great motivator and support, and Margaret Berstad for conversations and structuring insights. Lastly, I want to thank Ingunn Hanson for being endlessly supportive and kind, and Kasper for always keeping my mood up.

CONTENTS

Abstract **i**

Sammendrag **iii**

Preface **v**

Contents **viii**

List of Figures **viii**

List of Tables **xi**

Abbreviations **xiii**

1 Introduction **1**
- 1.1 Motivation . . . 1

2 Theory/Methods **3**
- 2.1 The PVS as an annular tube . . . 3
- 2.2 Model reduction . . . 3
  - 2.2.1 Continuity equation . . . 4
  - 2.2.2 Momentum Equation . . . 5
- 2.3 Outer Wall Mechanics . . . 7
- 2.4 Inner Wall Movement . . . 7
- 2.5 Numerical Scheme . . . 7
- 2.6 Characteristic analysis and BCs . . . 8
- 2.7 Test Setup . . . 10
- 2.8 Mass conservation . . . 11

3 Results **13**
- 3.1 Flow rate, Pressure and Area . . . 13
- 3.2 Flow characteristics . . . 14
- 3.3 Mass conservation . . . 17
- 3.4 Outer wall movement . . . 17
- 3.5 CFL-number and stability . . . 17

4 Discussion **19**
4.1 Choice of model geometry 19
4.2 Model reduction assumptions 20
4.3 Boundary conditions and inner wall movement 20
4.4 Stability 21

5 Conclusions **23**

References **25**

LIST OF FIGURES

2.7.1 Overview of the test setup. (a)Geometry and physical parameters for the PVS model as a hollow annular cylinder with an elastic outer wall, (b)applied inner wall motion, and (c)assumed flow profile s(r) for an axial cross-section. The figure was made using Inkscape. . . . 10

3.1.1 Area, flow rate and pressure at inlet, midpoint, and outlet, over 3 cycles of wall movement for the mouse dimensions. 13
3.1.2 Area, flow rate and pressure at inlet, midpoint, and outlet, over 3 cycles of wall movement for the human dimensions. 14
3.1.3 Pressure curve snapshots as R_1 goes from $R_{1,0}$ to $R_{1,max}$ in the 2nd cycle. The solid line is for the mouse trials, and the dashed line is for human trials. (a)-(d)Number of cycles=$[1, 1\frac{1}{12}, 1\frac{1}{6}, 1\frac{1}{4}]$. 15
3.1.4 Flow rate snapshots along the PVS as R_1 goes from $R_{1,0}$ to $R_{1,max}$ in the 2nd cycle, for the mouse trials. (a)-(d)Number of cycles=$[1, 1\frac{1}{12}, 1\frac{1}{6}, 1\frac{1}{4}]$. 15
3.1.5 Flow rate snapshots along the PVS as R_1 goes from $R_{1,0}$ to $R_{1,max}$ in the 2nd cycle, for the human trials. (a)-(d)Number of cycles=$[1, 1\frac{1}{12}, 1\frac{1}{6}, 1\frac{1}{4}]$. 16
3.3.1 Max difference and Root Mean Squares difference between PVS volume and total inflow as endpoints are removed. 17

LIST OF TABLES

2.2.1 Notation used to describe the domain 4
2.7.1 List of dimensions for the penetrating artery PVS used in the mouse and human systems 10
2.7.2 Overview of model parameters 11

3.2.1 Peak Reynold's Numbers and range of Womersley numbers for all trials. 16
3.2.2 Comparison of peak velocity for all trials at inlet node, i=0, and i=4. The peak velocity at the inlet is up to 3.23 times higher than at i=4 in the mouse dimensions (M-3), versus 1.34 for the human dimensions (H-10). 16
3.3.1 Max difference as a percentage of initial domain volume Δ_{max}/V^0_{PVS} for $f = 0.1$ in mouse and human dimensions, at nodes i=[0, 1, 2, 3, 4]. 17

ABBREVIATIONS

CSF	Cerebrospinal fluid
PVS	Perivascular space
1D	1-dimensional
PDE	Partial differential equation
ECS	Extracellular space
M-x	Trial in the mural PVS for frequency x=[0.1, 1, 3, 10]
H-x	Trial in the human PVS for frequency x=[0.1, 1, 3, 10]
CFL	Courant–Friedrichs–Lewy number

CHAPTER
ONE

INTRODUCTION

1.1 Motivation

Waste clearance is imperative for a healthy brain. Neurodegenerative disorders like Alzheimer's and Parkinson's disease have been connected to buildup of waste proteins like β-amyloid α-synuclein[1], yet the underlying mechanics of this transport is largely unknown. Formerly, it was thought that diffusion processes were the primary drivers of waste clearance, but in 2012-2013, a series of studies [2] [3] [4] described the glymphatic system, where cerebrospinal fluid (CSF) is produced and transported along penetrating arteries, before being transported into the brain tissue by glial cells and removed from the central nervous system through lymphatic pathways. The Glymphatic System has since been the leading model for the transport of cerebrospinal fluid and interstitial solutions through the brain. A major contributor to this circulation is the transport of CSF along perivascular spaces (PVS) surrounding the brain vasculature. Although the transport of particles along the PVS is well documented [5][6][7], the underlying physical mechanisms causing directional flow in these are not well understood. Hadaczek et al. [8] proposed peristaltic pumping as a major mechanism, while the effect of vasomotion [9] and functional hyperemia [10][11] have also been studied. Gan et al.[12] explored the idea of pressure dependent permeability of the outer wall of the PVS around a penetrating artery, increasing the CSF flow into the brain tissue as the blood vessel expands, causing inflow from the pial artery PVS when the vessel contracts.

Although imaging techniques are being improved, studying perivascular flow *in vivo* is challenging, and the use of mathematical modeling and simulation is important for PVS flow research. 3-dimensional flow simulations in complex systems of vessels are both expensive and time-consuming, so simplified models are more practical. When calculating flow in complex structures of blood-vessels, reduced 1-dimensional (1D) models are commonly used, and have been shown to be accurate[13]. The book “Mathematical Modeling and Numerical Simulation of the Cardiovascular System” by Quarteroni and Formaggia is a comprehensive guide to describing blood flow in compliant vessels, and my first goal is to follow their approach and make a 1-dimensional model of CSF flow in an annular PVS due to arterial pulsations. To achieve this, I will first reduce the incompressible Navier-Stokes Equations for Newtonian flow in a deformable domain to a set of 1-dimensional partial differential equations (PDEs) by integration over a PVS-shaped control volume using cross-secionally averaged flow-values. Then I will write a python-program to solve this set of equations using a MacCormack scheme.

My second goal is to use this model to investigate the flow characteristics, with focus on flow rate, pressure variation, axial pressure gradient, Reynold's numbers and Womersley numbers of a mural and human penetrating arteriole PVS during pulsations caused by vasomotion and a range or heart rates.

CHAPTER

TWO

THEORY/METHODS

2.1 The PVS as an annular tube

The PVS is the space surrounding the brain vasculature. It is filled with CSF and is bound by the vessel wall on the inside and a layer of astrocyte endfeet separating it from the extracellular space (ECS) on the outside. The astrocyte endfeet are connected with gap junctions through which CSF can flow into the ECS. The PVS shape varies for different types of arteries, being elliptical for the subarachnoid vessel and nearly circular for penetrating arterioles [1]. Mural PVS surrounding surface arteries are measured to be about 20-40μm wide and open as opposed to porous[14], while penetrating arteriole PVSs are smaller[15].

2.2 Model reduction

The goal of the current section is to arrive at a system of 1-dimensional PDEs governing the flow in a straight, cylindrical PVS. The derivation is included for completeness and ease of reading. I will be following the steps of Quarteroni and Formaggia[16] closely, using mostly their notation, and commenting on adjustments needed to account for the differences of an annular domain. I begin by making the following assumptions:

1. Axial symmetry: All quantities are independent of the angular coordinate θ. Every axial section $z = const$ remains circular during the wall motion. The inner and outer radii, R_1 and R_2 are a function of only z and t

2. Radial displacements of boundaries: The walls displace along the radial direction solely. We may write $\eta_i = \eta_i \mathbf{e}_r$, $i = 1, 2$, where $\eta_i = R_i - R_{i,0}$ is the displacement of the inner and outer wall respectively.

3. Constant pressure: We assume that the pressure P is constant on each section, so that it depends only on z and t

4. No body forces: We neglect body forces, thus $\mathbf{f} = \mathbf{0}$ in the momentum equation

5. Dominance of axial velocity: The velocity components orthogonal to the z axis are negligible compared to the component along z, u_z, which will be simplified as $u_z(t,r,z) = \bar{u}(t,z)s(r)$, where $\bar{u}(t,s)$ is the mean velocity over the axial section and $s(r)$ is an assumed velocity profile.

These are the same as the ones used when deriving the arterial flow model in [16], with the addition of the subscript in assumption 2, to account for the addition of an inner wall. The velocity profile in assumption 5 is given as a function of the radius, $s(r)$ as opposed to the normalized radius $s(r/R)$ in [16]

Under these assumptions, the incompressible Navier-Stokes Equations reduce to

$$\text{div}(\mathbf{u}) = 0 \tag{2.1}$$

$$\frac{\partial u_z}{\partial t} + \text{div}(u_z \mathbf{u}) + \frac{1}{\rho}\frac{\partial P}{\partial z} - v\Delta u_z = 0 \tag{2.2}$$

where ρ is the CSF density, ν is the kinematic viscosity and $\Delta = \nabla^2$ is the Laplace operator. The next step is to integrate equations 2.1 and 2.2 over the control volume, starting with the mass equation. An overview of the notation used is given in Table 2.2.1

Spatial domain:	Ω_t
Domain boundary	$\partial\Omega$
Section of Ω_t	$\mathcal{P}$
Section boundary	$\partial\mathcal{P}$
Wall boundary of Ω	Γ_t^w
Generic axial section	$\mathcal{S}$

Table 2.2.1: Notation used to describe the domain

2.2.1 Continuity equation

Integrating the mass equation (Eq. 2.1) over a section $\mathcal{P}$ of the domain Ω_t and using the divergence theorem gives:

$$0 = \int_{\mathcal{P}} \text{div}(\mathbf{u}) = \int_{\mathcal{S}^-} u_z + \int_{\mathcal{S}^+} u_z + \int_{\Gamma_{\mathcal{P}}^w} \mathbf{u}\cdot\mathbf{n} \tag{2.3}$$

$\mathcal{S}^-$ and $\mathcal{S}^+$ signify the part of the boundary lying on the left, and right axial plane respectively. $\Gamma_{\mathcal{P}}^w$ is the wall boundary of $\mathcal{P}$ and $\mathbf{n}$ is the outward normal to the boundary. Due to the no-slip condition by the walls, the velocity $\mathbf{u} = \dot{\eta}\mathbf{e}_r$. Additionally, since the PVS has both an inner and an outer wall, the last term can be written as:

$$\int_{\Gamma_{\mathcal{P}}^w} \mathbf{u}\cdot\mathbf{n} = \int_{\Gamma_{\mathcal{P},1}^w} (-1)\dot{\eta}_1 + \int_{\Gamma_{\mathcal{P},2}^w} \dot{\eta}_2 = [2\pi(R_2\dot{\eta}_2 - R_1\dot{\eta}_1)dz + \mathcal{O}(dz^2)] \tag{2.4}$$

subscript 1 and 2 signifying the inner and outer wall. Using the ALE-theorem for a function f=1 lets me describe the change in area due to each wall movement as

$$\frac{\partial A_i}{\partial t} = 2\pi R\dot{\eta} \tag{2.5}$$

making the total area change

$$\frac{\partial A}{\partial t} = 2\pi(R_2\dot{\eta}_2 - R_1\dot{\eta}_1) \tag{2.6}$$

$$\int_{\mathcal{S}^-} u_z + \int_{\mathcal{S}^+} u_z = 2\pi\frac{\partial u}{\partial z}\,dz \tag{2.7}$$

and as dz→0, Equation 2.3 becomes the Continuity Equation

$$\frac{\partial A}{\partial t} + \frac{\partial Q}{\partial z} = 0 \tag{2.8}$$

Although Equation 2.4 introduces an extra term for the inner wall, the resulting Continuity Equation (Eq.2.8) is the same as in [16], as the inner wall contribution to area change is accounted for in Equation 2.6 and is a part of $\frac{\partial A}{\partial t}$.

2.2.2 Momentum Equation

The next step is to handle the momentum equation (Eq 2.2). Still following [16], I integrate each term over $\mathcal{P}$, starting with:

$$\int_{\mathcal{P}} \frac{\partial u}{\partial t} = \frac{d}{dt}\int_{\mathcal{P}} u_z - \int_{\partial\mathcal{P}} u_z \mathbf{w}\cdot\mathbf{n} = \frac{d}{dt}\int_{\mathcal{P}} u_z \tag{2.9}$$

where $\mathbf{w}$ is the velocity of the boundary of $\mathcal{P}$. The boundary integral is equal to 0, as $\mathbf{w} = 0$ at $\mathcal{S}^-$ and $\mathcal{S}^+$, while $u_z = 0$ at the wall. Using the definition of the average velocity, $\bar{u}$ we can write.

$$\boxed{\int_{\mathcal{P}} \frac{\partial u}{\partial t} = \frac{d}{dt}\int_{\mathcal{P}} u_z = \frac{\partial}{\partial t}[A\bar{u}\,dz + \mathcal{O}(dz^2)]} \tag{2.10}$$

Next is the term

$$\int_{\mathcal{P}} \operatorname{div}(u_z\vec{u}) = \int_{\partial\mathcal{P}} u_z\mathbf{u}\cdot\mathbf{n} = -\int_{\mathcal{S}^-} u_z^2 + \int_{\mathcal{S}^+} u_z^2 + \int_{\Gamma_{\mathcal{P}}^w} u_z\mathbf{w}\cdot\mathbf{n} \tag{2.11}$$

Again, the wall boundary integral = 0, and by introducing the Coriolis coefficient:

$$\alpha = \frac{\int_{\mathcal{S}} u_z^2\,d\sigma}{A\bar{u}^2} \tag{2.12}$$

we can write:

$$\boxed{\int_{\mathcal{P}} \operatorname{div}(u_z\vec{u}) = -\int_{\mathcal{S}^-} u_z^2 + \int_{\mathcal{S}^+} u_z^2 = \frac{\partial}{\partial z}(\alpha A\bar{u}^2)dz + \mathcal{O}(dz^2)} \tag{2.13}$$

Again, the terms accounting for the addition of the inner wall

Assuming constant pressure on each axial section, the pressure term can be written as

$$\int_{\mathcal{P}} \frac{\partial P}{\partial z} = -\int_{\mathcal{S}^-} P + \int_{\mathcal{S}^+} P + \int_{\Gamma_{\mathcal{P}}^w} P\,n_z \tag{2.14}$$

because $\int_{\partial\mathcal{P}} n_z = 0$, we can write rewrite the last term as

$$\int_{\Gamma^w_{\mathcal{P}}} P\, n_z = P\int_{\Gamma^w_{\mathcal{P}}} n_z + \mathcal{O}(dz^2) = -P\int_{\partial\mathcal{P}\setminus\Gamma^w_{\mathcal{P}}} n_z + \mathcal{O}(dz^2) = -P\frac{\partial A}{\partial z}\, dz + \mathcal{O}(dz^2) \tag{2.15}$$

Similarly,

$$-\int_{\mathcal{S}^-} P + \int_{\mathcal{S}^+} P = \frac{\partial AP}{\partial z}\, dz + \mathcal{O}(dz^2) \tag{2.16}$$

and inserting them back into Equation 2.14 and using the chain rule we can write

$$\boxed{\int_{\mathcal{P}} \frac{\partial P}{\partial z} = \Big(\frac{\partial AP}{\partial z} - P\frac{\partial A}{\partial z}\Big)\, dz + \mathcal{O}(dz^2) = A\frac{\partial P}{\partial z}\, dz + \mathcal{O}(dz^2)} \tag{2.17}$$

Lastly, we have the viscous term, which due to the divergence theorem can be rewritten as:

$$\int_{\mathcal{P}} \Delta u_z = \int_{\partial\mathcal{P}} \nabla u_z \cdot \mathbf{n} = -\int_{\mathcal{S}^-} \frac{\partial u_z}{\partial z} + \int_{\mathcal{S}^+} \frac{\partial u_z}{\partial z} + \int_{\Gamma^w_{\mathcal{P}}} \nabla u_z \cdot \mathbf{n} \tag{2.18}$$

The axial variation of $\frac{\partial u_z}{\partial z}$ is small compared to the last term, and is neglected. Additionally, $\nabla u_z \cdot \mathbf{n} = \frac{\partial u_z}{\partial r} n_r \mathbf{e}_r$ as $\frac{\partial u_z}{\partial \theta} = 0$, and $\frac{\partial u_z}{\partial z}\, n_z$ is proportional to $\partial u_z/\partial z$, and we can write

$$\int_{\Gamma^w_{\mathcal{P}}} \frac{\partial u_z}{\partial r} n_r = \int_{\Gamma^w_{\mathcal{P},1}} \frac{\partial u_z}{\partial r} n_r + \int_{\Gamma^w_{\mathcal{P},2}} \frac{\partial u_z}{\partial r} n_r \tag{2.19}$$

where $\Gamma^w_{\mathcal{P},1}$ and $\Gamma^w_{\mathcal{P},1}$ are the inner and outer wall boundaries. Since $u_s = \bar{u}s(r)$ and using the relation $n_r\, d\sigma = 2\pi R\, dz$, the terms can be rewritten in

$$\begin{aligned} \int_{\Gamma^w_{\mathcal{P},1}} \frac{\partial u_z}{\partial r} n_r &= \int_{\Gamma^w_{\mathcal{P},1}} \bar{u}s'(R_1) n_r d\sigma \approx -2\pi\bar{u}(s^*)s'(R_1)R_1 dz \\ \int_{\Gamma^w_{\mathcal{P},2}} \frac{\partial u_z}{\partial r} n_r &= \int_{\Gamma^w_{\mathcal{P},2}} \bar{u}s'(R_2) n_r d\sigma \approx 2\pi\bar{u}(s^*)s'(R_2)R_2\, dz \end{aligned} \tag{2.20}$$

and the viscosity term becomes

$$\boxed{\int_{\mathcal{P}} \Delta u_z = 2\pi(R_2 s'(R_2) - R_1 s'(R_1))dz} \tag{2.21}$$

Inserting the boxed equations back into Equation 2.9, dividing by dz and letting $dz \to 0$, what remains is the momentum equation:

$$\frac{\partial Q}{\partial t} + \alpha\frac{\partial}{\partial z}\Big(\frac{Q^2}{A}\Big) + \frac{A}{\rho}\frac{\partial P}{\partial z} + K_r\Big(\frac{Q}{A}\Big) = 0 \tag{2.22}$$

Where $K_r = -2\pi\nu(R_2 s'(R_2) - R_1 s'(R_1))$ is the friction parameter resulting from the viscosity term in Eq.2.21.

With this, we have arrived at the 1-dimensional Continuity and Momentum Equations. I note that despite the inclusion of the inner wall, the resulting equations only differ from those of the simple compliant vessel by the friction factor K_r.

2.3 Outer Wall Mechanics

To describe the movement of the outer wall, I'm using the Independent Ring Model described in section 16.2 of [16]:

$$\begin{aligned}
&\frac{\partial^2 \eta_2}{\partial t^2} + b\eta_2 = H \\
&b = \frac{E}{\rho_w (1-\xi^2) R_{2,0}^2} \\
&H = \frac{1}{\rho_w h}\Big[\frac{R_2}{R_{2,0}}(P - P_{ext}) - 2g\big(\vec{D}(\vec{u}\cdot\vec{n})\big)\cdot\vec{e_r}\Big]
\end{aligned} \tag{2.23}$$

ρ_w being the wall density, $g = \frac{R_2}{R_{2,0}}\sqrt{1 + (\frac{1}{R_2}\frac{\partial R_2}{\partial \theta})^2 + (\frac{\partial R_2}{\partial z})^2}$, and $\vec{D}$ being the Strain Rate Tensor. The added subscript in the radius and wall movement variables signifies that they're regarding the outer wall. The H-term is often simplified by assuming $\frac{R}{R_0} \approx 1$ and neglecting the contribution from viscous forces, leaving $H = \frac{P-P_{ext}}{\rho_w h}$. By also neglecting the acceleration term, Equation 2.23 can be written as:

$$\frac{E}{(1-\xi^2)R_{2,0}^2}\eta_2 = \frac{P - P_{ext}}{h_2}, \tag{2.24}$$

which rearranged gives:

$$P - P_{ext} = \frac{h_2 E}{(1-\xi^2)R_{2,0}^2}\eta_2 \tag{2.25}$$

The pressure can be described by the change in area by re-arranging the relation $A = \pi\big((R_{2,0} + \eta_2)^2 - R_1^2\big)$, and substituting for η_2 in Equation 2.25 giving:

$$P - P_{ext} = \frac{h_2 E}{(1-\xi^2)R_{2,0}^2}\Big(\sqrt{\frac{A}{\pi} + R_1^2} - R_{2,0}\Big) \tag{2.26}$$

I choose the reference pressure at $R_2 = R_{2,0}$ as $P_0 = P_{ext} = 0$.

2.4 Inner Wall Movement

The movement of the inner wall is applied by updating R_1 in the constitutive equation 2.26 for each time step, using a predetermined function $R_1(t)$. In the current test-configuration, $R_1 = R_{1,0}\big(1 + 0.025\sin(2\pi f t)\big)$(Figure.2.7.1(b))

2.5 Numerical Scheme

To solve the system of equations (2.8,2.22) I use a MacCormack scheme[17]. Writing the system of equations (2.8 and 2.22) in conservative form:

$$\frac{\partial \mathbf{U}}{\partial t} + \frac{\partial \mathbf{F}}{\partial z} + \mathbf{S} = \mathbf{0}. \tag{2.27}$$

A MacCormack scheme consists of a prediction and correction step on the form:

$$\begin{aligned}\mathbf{U}_i^p =& \mathbf{U}_i^n - \frac{\Delta t}{\Delta x}(\mathbf{F}_{i+1}^n - \mathbf{F}_i^n) - \Delta t \mathbf{S}_i^n \\ \mathbf{U}_i^{n+1} =& \frac{\mathbf{U}_i^n + \mathbf{U}_i^p}{2} - \frac{\Delta t}{2\Delta x}(\mathbf{F}_i^p - \mathbf{F}_{i-1}^p) + \frac{\Delta t}{4}(\mathbf{S}_i^n - \mathbf{S}_i^p)\end{aligned} \tag{2.28}$$

Since the area in $\frac{A}{\rho}\frac{\partial P}{\partial z}$ from Equation 2.22 isn't a part of the differentiation, Fossan[18] argues for the use of a quasi-conservative form where, the area is in this step is treated as constant and one value of is chosen for both flux terms $\mathbf{F}_{i-1}^n$ and $\mathbf{F}_i^n$ in Equation 2.28. The quasi-conservative form is written as:

$$\mathbf{U}' = \begin{bmatrix} A \\ Q \end{bmatrix}, \ \mathbf{F}' = \begin{bmatrix} Q \\ \frac{\alpha Q^2}{A} + \frac{A_c P}{\rho} \end{bmatrix}, \ \mathbf{S}' = \begin{bmatrix} 0 \\ K_r\left(\frac{Q}{A}\right) \end{bmatrix}. \tag{2.29}$$

where A_c signifies the area not part of the differentiation. It is chosen to be evaluated at point i, and he notes that it is not given at which point the area should be evaluated, but that the effect of this choice is likely not big, as the wavelength in general is long in physical conditions[18].

The resulting altered numerical scheme is:

$$\begin{aligned}\mathbf{U}_i^p &= \mathbf{U}_i^n - \frac{\Delta t}{\Delta x}(\mathbf{F}_{i+1}^n\big|_{A_c} - \mathbf{F}_i^n\big|_{A_c}) + \Delta t \mathbf{b}_i^n \\ \mathbf{U}_i^{n+1} &= \frac{\mathbf{U}_i^n + \mathbf{U}_i^p}{2} - \frac{\Delta t}{2\Delta x}(\mathbf{F}_i^p\big|_{A_c} - \mathbf{F}_{i-1}^p\big|_{A_c}) + \frac{\Delta t}{4}(\mathbf{b}_i^n + \mathbf{b}_i^p)\end{aligned} \tag{2.30}$$

2.6 Characteristic analysis and BCs

Equations 2.8 and 2.22 can also be written in the non-conservative form as:

$$\frac{\partial \mathbf{U}}{\partial t} + \mathbf{H}\frac{\partial \mathbf{U}}{\partial z} + \mathbf{B} = 0 \tag{2.31}$$

$$\mathbf{U} = \begin{bmatrix} A \\ Q \end{bmatrix}, \ \mathbf{H} = \begin{bmatrix} 0 & 1 \\ c^2 - \left(\frac{\alpha Q}{A}\right)^2 & 2\alpha\frac{\alpha Q}{A} \end{bmatrix}, \ \mathbf{B} = \begin{bmatrix} 0 \\ K_r\frac{Q}{A} \end{bmatrix} \tag{2.32}$$

where $c = \sqrt{\frac{A}{\rho}\frac{\partial P}{\partial A}}$ is the celerity. The **B**-term was simplified by assuming A_0 and β to be constant along the z-axis. The matrix **H** can be diagonalized as $\mathbf{H} = \mathbf{R\Lambda L}$, where $\mathbf{R} = \begin{bmatrix}\mathbf{r_1} & \mathbf{r_2}\end{bmatrix}$, $\mathbf{L} = \begin{bmatrix}\mathbf{l_1}^T \\ \mathbf{l_2}^T\end{bmatrix}$ are the right and left eigenvector matrices of **H**, satisfying $\mathbf{LR} = \mathbf{I}$, and $\Lambda = \begin{bmatrix}\lambda_1 & 0 \\ 0 & \lambda_2\end{bmatrix}$ contains the eigenvalues. Eqs.2.31 can then be rewritten as

$$\mathbf{L}\frac{\partial \mathbf{U}}{\partial t} + \mathbf{\Lambda L}\frac{\partial \mathbf{U}}{\partial z} + \mathbf{LB} = 0 \tag{2.33}$$

By defining characteristic variables:

$$W_1 = \frac{\partial W_1}{\partial \mathbf{U}} = \mathbf{l_1}, \qquad W_2 = \frac{\partial W_2}{\partial \mathbf{U}} = \mathbf{l_2} \tag{2.34}$$

constructing a new matrix $\mathbf{W} = [W_1, W_2]^T$, and assuming $\mathbf{B} = 0$, Equation 2.33 further simplifies to

$$\frac{\partial W_i}{\partial t} + \lambda_i \frac{\partial W_i}{\partial z} = 0 \tag{2.35}$$

which describes a system where W_1 and W_2 are constant along the characteristic paths $\frac{\partial z}{\partial t} = \lambda_1$ and $\frac{\partial z}{\partial t} = \lambda_2$ respectively.

For Eq.2.31, we find that the left and right eigenmatrices become:

$$\mathbf{R} = \frac{A}{2c}\begin{bmatrix} 1 & -1 \\ \lambda_1 & -\lambda_2 \end{bmatrix}, \qquad \mathbf{L} = \frac{1}{A}\begin{bmatrix} -\lambda_2 & 1 \\ -\lambda_1 & 1 \end{bmatrix} \tag{2.36}$$

with eigenvalues $\lambda_{1,2} = U \pm c$ for $\alpha = 1$. The celerity is given by:

$$c = \sqrt{\frac{A\beta}{2\pi\rho\sqrt{A/\pi + R_1^2}}}, \qquad \beta = \frac{h_2 E}{(1-\xi^2)R_{2,0}^2} \tag{2.37}$$

Flows in the body are generally subcritical, $U < c$, meaning the characteristics travel in opposite directions, and we can categorize them as incoming and outgoing.

The value of the characteristic variables can be found by integrating the definition (Eq. 2.34) giving:

$$\Delta\mathbf{W} = \int \mathbf{L}\, d\mathbf{U} \tag{2.38}$$

Inserting values from Equation 2.36 into Eq. 2.38, integrating over a time-step and using the mean-value theorem, we get the relation:

$$\begin{aligned} \Delta W_1 &= L_{11}\Delta A + L_{12}\Delta Q \\ \Delta W_2 &= L_{21}\Delta A + L_{22}\Delta Q \end{aligned} \tag{2.39}$$

and conversely:

$$\begin{aligned} \Delta A &= R_{11}\Delta W_1 + R_{12}\Delta W_2 \\ \Delta Q &= R_{21}\Delta W_1 + R_{22}\Delta W_2 \end{aligned} \tag{2.40}$$

The outlet boundary condition of no reflections is set by prescribing $W_2 = 0$, and the condition of $P = 0$ at the inlet is set by prescribing ΔA based on the change of R_2 and R_1 in the incoming characteristic.

2.7 Test Setup

I test the model on two sets of dimensions, representing the penetrating arteriole PVS of a mouse and human, respectively. For the mouse PVS, the length of the PVS $L = 1\,mm$, arteriole initial radius $R_{1,0} = 10\,\mu m$, outer wall initial radius $R_{2,0} = 20\,\mu m$ and outer wall thickness $h = 3\,\mu m$, which are common values for a mouse arteriole PVS[19][20]. For simplicity and ease of comparison, the human PVS is represented by a 5x upscaling of the mouse PVS, making the arteriole radius, $R_1 = 50\,\mu m$, which matches a human penetrating arteriole[21]. A complete list of the domain dimensions is given in Table 2.7.1.

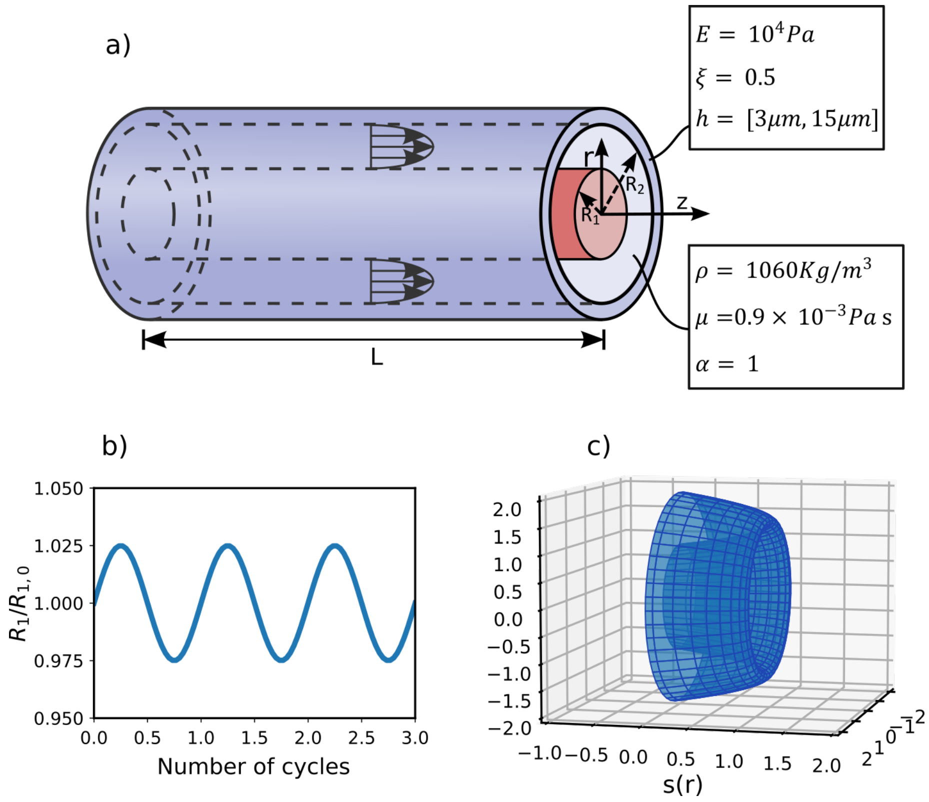
a)
$E = 10^4 Pa$
$\xi = 0.5$
$h = [3\mu m, 15\mu m]$
r
R_2
R_1
z
$\rho = 1060 Kg/m^3$
$\mu = 0.9 \times 10^{-3} Pa\,s$
$\alpha = 1$
L
b)
1.050
1.025
1.000
0.975
0.950
$R_1/R_{1,0}$
0.0
0.5
1.0
1.5
2.0
2.5
3.0
Number of cycles
c)
2.0
1.5
1.0
0.5
0.0
−0.5
−1.0
−1.5
−2.0
−1.0
−0.5
0.0
0.5
1.0
1.5
2.0
s(r)
2
1
0
−1
2

Figure 2.7.1: Overview of the test setup. (a)Geometry and physical parameters for the PVS model as a hollow annular cylinder with an elastic outer wall, (b)applied inner wall motion, and (c)assumed flow profile s(r) for an axial cross-section. The figure was made using Inkscape.

	Mouse	Human
Domain length, L	1 mm	5 mm
Initial radius inner wall, $R_{1,0}$	$10\mu m$	$50\mu m$
Initial radius outer wall, $R_{2,0}$	$20\mu m$	$100\mu m$
Outer wall thickness, h	$3\mu m$	$15\mu m$
CFL number	0.8	0.9

Table 2.7.1: List of dimensions for the penetrating artery PVS used in the mouse and human systems

CSF density, ρ	$1060 Kg/m^3$
Dynamic viscosity, μ	$0.9 \times 10^{-3} Pa \cdot s$
Young's modulus, E	$10^4 Pa$
Poisson's ratio, ξ	0.5
Coriolis coefficient, α	1
Spatial nodes, nz	51

Table 2.7.2: Overview of model parameters

For both setups, the wall movement is described by $R_1 = R_{1,0}(1{+}0.025 sin(2\pi f t))$(Figure 2.7.1b), with $f = [0.1, 1, 3, 10]$. $f = 0.1$ roughly represents vasomotion[22], $f = 1$ and $f = 3$ represents a human heartbeat at rest and heavy exercise, and f=10 represents a mural heartbeat[22]. The CSF is modeled as water with density $\rho = 1060 Kg/m^3$ and dynamic viscosity $\mu = 0.9 \times 10^{-3} Pa \cdot s$. The outer wall is modeled as incompressible, $\xi = 0.5$ and Young's modulus $E = 10^4 Pa$[23].

The number of spacial nodes $nz = 51$, making $\Delta z = [20\mu m, 100\mu m]$. Δt is given by the Courant-Friedrichs-Lewy condition $cfl = \frac{\Delta t}{\Delta z}\left(|u| + c\right)_{max}$[24]. I assume the normalized annular Poiseuille flow profile used by Daversin-Catty[25], shown in Figure 2.7.1c, given by:

$$\begin{aligned} v_{vp}(r) =& \frac{v_{poise(r)}}{v_{poise}\left(\frac{R_1+R_2}{2}\right)} \\ v_{poise}(r) =& \left(1 - \frac{r^2}{R_1^2} + \frac{R_2^2 - R_1^2}{R_1^2 \ln(R_2/R_1)}\right) \end{aligned} \tag{2.41}$$

An overview of model parameters is found in Table 2.7.2. For completeness, I run all frequencies on both sized setups.

2.8 Mass conservation

Due to unforeseen results close to the domain boundaries, described in 3.1, I also conduct a mass conservation test. The PVS volume $V_{PVS}^n = \int_{i=0}^{nz} A^n \, dz$ is approximated for each time step using Simpson's integration, and the total volume flow entering the PVS, $Q_{tot} = \int_0^{t^n} q \, dt$, is approximated using cumulative trapezoids. To quantify the discrepancy, I use Root mean square deviation:

$$\Delta_{RMS} = \sqrt{\frac{\sum_{n=1}^{nt}(Q_{tot}^n - \Delta V^n)^2}{nt}} \tag{2.42}$$

where $\Delta V^n = V_{PVS}^n - V_{PVS}^0$ is the total change in PVS volume at the n'th time step and nt is the total number of time steps. I also measure the maximum deviation $\Delta_{max} = (Q_{tot} - \Delta V)_{max}$ for each trial. To investigate the boundary nodes' effect on the results, the mass conservation test is repeated while iteratively removing 1–4 nodes from each side.

CHAPTER

THREE

RESULTS

3.1 Flow rate, Pressure and Area

In Figure 3.1.1, the PVS cross-section area, CSF flow rate and CSF pressure is plotted for the PVS inlet, midpoint, and outlet for M-0.1–M-10. The area fluctuated with a similar pattern around a_0 for all frequencies, with an amplitude gradually decreasing from inlet through to outlet. The flow rate at the inlet reached a steady oscillation around $q = 0mm^3/s$ after half a cycle, with amplitudes varying exponentially with frequency. The flow rates at the midpoint were similar in amplitude for all frequencies, while at the outlet, the amplitudes were slightly differentiated with lower amplitudes for higher frequencies. At the midpoint, the pressure fluctuated in a similar pattern for all frequencies, with a slightly increased amplitude for M-10, while at the outlet, the pressure was identical for all frequencies.Both the flow rate-, pressure- and area curves show a positive phase shift along the PVS, most noticeable for M-10.

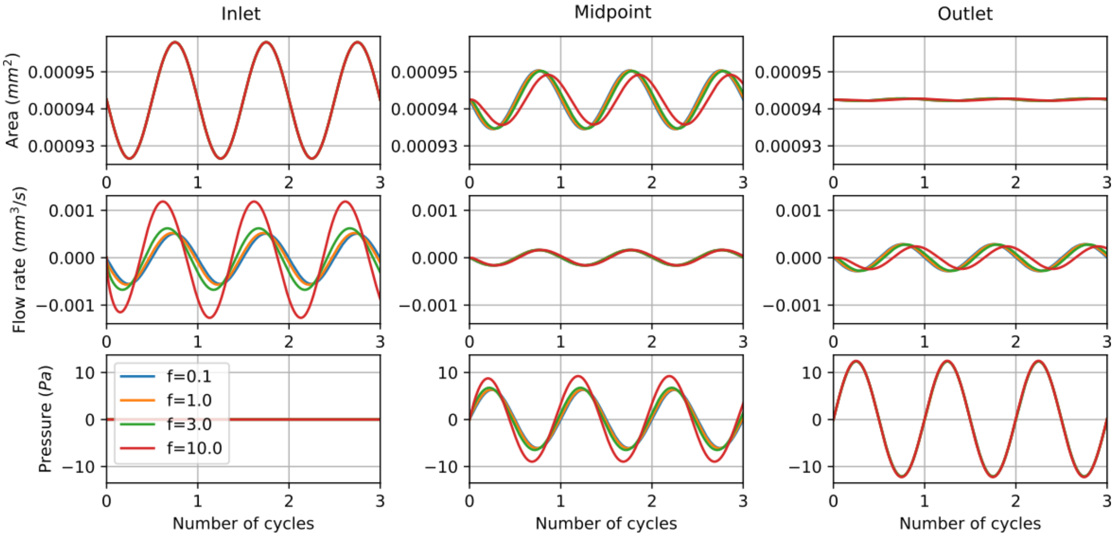

Figure 3.1.1: Area, flow rate and pressure at inlet, midpoint, and outlet, over 3 cycles of wall movement for the mouse dimensions.

Figure 3.1.2, shows the corresponding results for human dimensions. The resulting oscillations are very similar as in the mouse dimensions. At the inlet and midpoint, the area is increased by a factor of 25 and the flow rate by a factor of 50. At the outlet, the area and flow rate amplitudes are slightly higher relative to the midpoint, compared to the corresponding amplitudes for mouse dimensions. The pressure curves for all frequencies are close to identical to the corresponding pressure curves in the mouse dimensions.

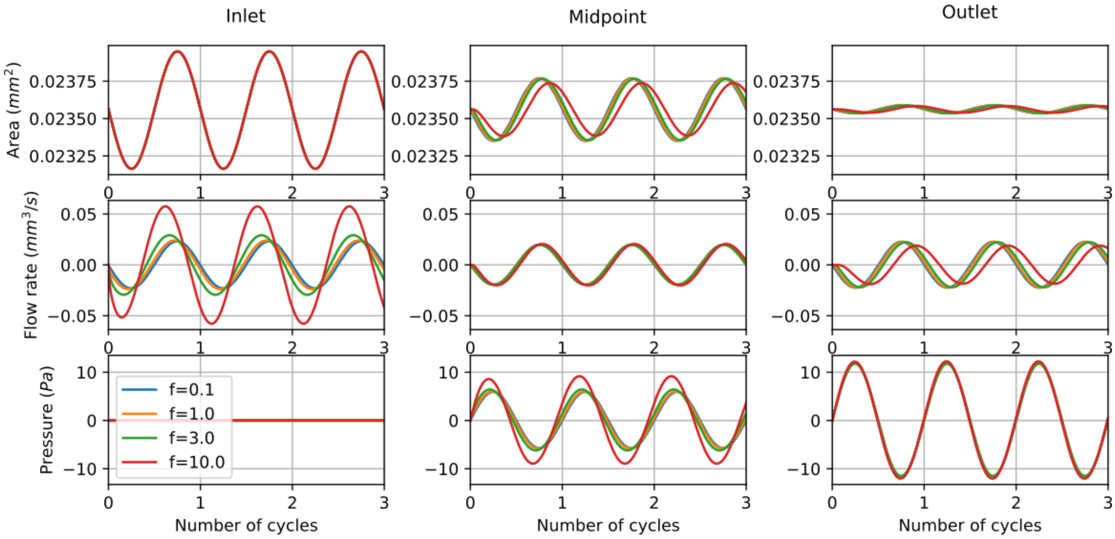

Figure 3.1.2: Area, flow rate and pressure at inlet, midpoint, and outlet, over 3 cycles of wall movement for the human dimensions.

Figure 3.1.3 shows the pressure profiles along the PVS for four equally spaced time-points as R_1 goes from $R_{1,0}$ to $R_{1_{max}}$, for both sets of dimensions. In (a), the pressure curves for M-0.1 and H-0.1 are close to flat at 0Pa along the PVS, while frequencies 1–10 Hz have increasingly curved pressure profiles. (b-d) show the curvatures of frequency 1–10 Hz become increasingly linear as the pressure approaches the peak values of approximately 12.5 Pa at the outlet. There is a slight deviation in the solution at the inlet and outlet, where the slope magnitude of the slope changes abruptly. The deviation appears reversely proportional to the slope magnitude.

Figure 3.1.4 and 3.1.5 show the corresponding flow rate profiles for mouse and human dimensions, respectively. At the boundaries in both ends of the PVS, the flow rate deviates from the rest of the solution for all trials. The deviation is consistently in the direction of the flow and appears proportional to the magnitude. The effect is considerably stronger in the smaller dimensions, where it at the inlet is present also in the neighboring nodes.

3.2 Flow characteristics

Table 3.2.1 shows peak Reynold's numbers and range of Womersley numbers for all trials. Peak pressure gradients: M:12.5Pa/mm and H:2.5Pa/mm over the domain. At peak pressure, the gradients were approximately constant.

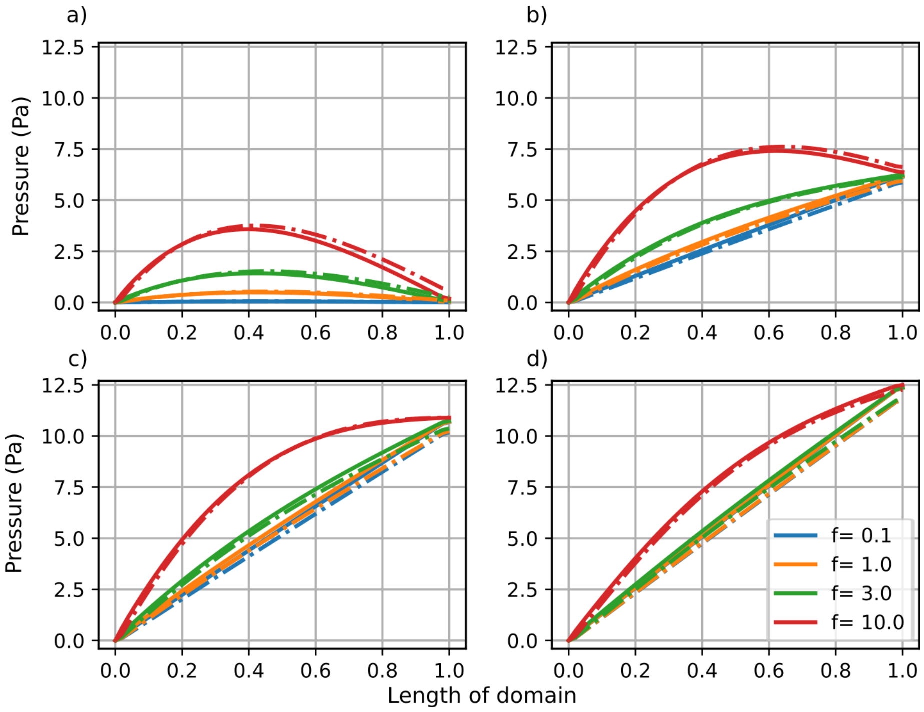

Figure 3.1.3: Pressure curve snapshots as R_1 goes from $R_{1,0}$ to $R_{1,max}$ in the 2nd cycle. The solid line is for the mouse trials, and the dashed line is for human trials. (a)-(d)Number of cycles=$[1, 1\frac{1}{12}, 1\frac{1}{6}, 1\frac{1}{4}]$.

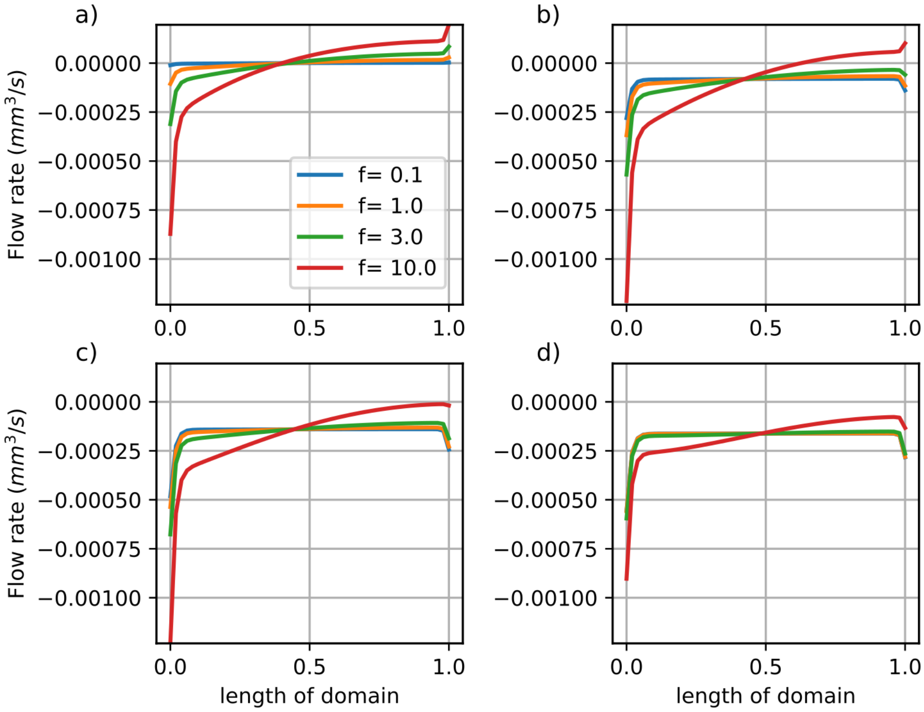

Figure 3.1.4: Flow rate snapshots along the PVS as R_1 goes from $R_{1,0}$ to $R_{1,max}$ in the 2nd cycle, for the mouse trials. (a)-(d)Number of cycles=$[1, 1\frac{1}{12}, 1\frac{1}{6}, 1\frac{1}{4}]$.

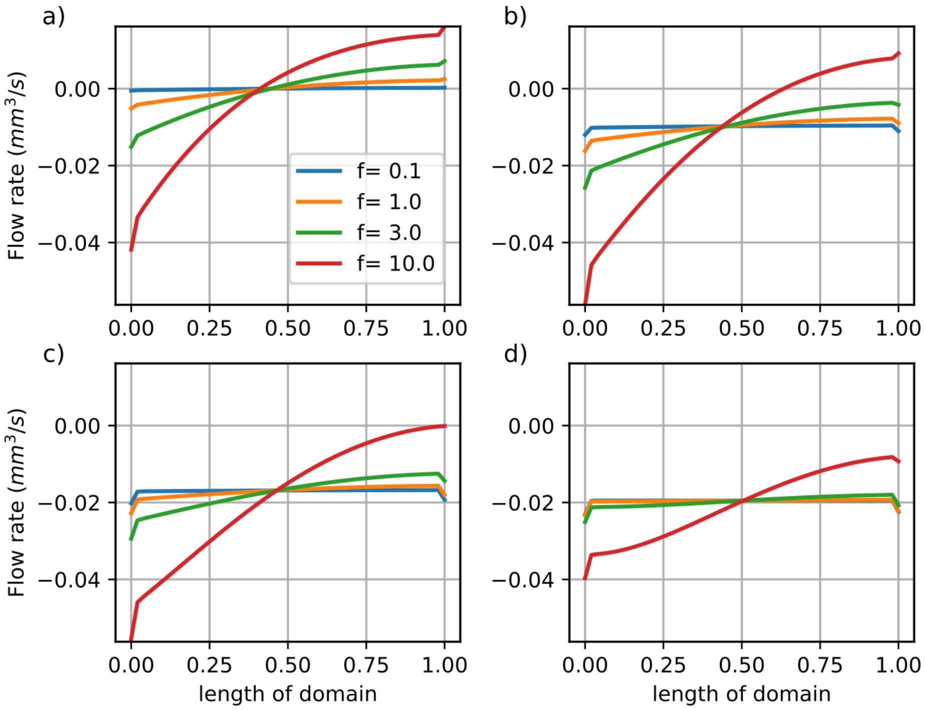

Figure 3.1.5: Flow rate snapshots along the PVS as R_1 goes from $R_{1,0}$ to $R_{1,max}$ in the 2nd cycle, for the human trials. (a)-(d)Number of cycles=$[1, 1\frac{1}{12}, 1\frac{1}{6}, 1\frac{1}{4}]$.

	Mouse		Human	
f	Re_{max}	Wo	Re_{max}	Wo
0.1	0.0133	[0.0161, 0.0183]	0.1214	[0.0808, 0.0916]
1	0.0137	[0.0511, 0.0579]	0.1252	[0.2556, 0.2896]
3	0.0162	[0.0885, 0.1003]	0.1519	[0.4426, 0.5016]
10	0.0306	[0.1616, 0.1832]	0.2971	[0.8082, 0.9158]

Table 3.2.1: Peak Reynold's Numbers and range of Womersley numbers for all trials.

	Mouse		Human	
	i=0	i=4	i=0	i=4
$f = 0.1$	0.531 mm/s	0.173 mm/s	0.968 mm/s	0.826 mm/s
$f = 1$	0.545 mm/s	0.177 mm/s	1.000 mm/s	0.846 mm/s
$f = 3$	0.651 mm/s	0.201 mm/s	1.222 mm/s	0.986 mm/s
$f = 10$	1.246 mm/s	0.352 mm/s	2.417 mm/s	1.784 mm/s

Table 3.2.2: Comparison of peak velocity for all trials at inlet node, i=0, and i=4. The peak velocity at the inlet is up to 3.23 times higher than at i=4 in the mouse dimensions (M-3), versus 1.34 for the human dimensions (H-10).

3.3 Mass conservation

Figure 3.3.1 shows the results from the mass conservation test. Both Δ_{max}. The peak value for the tests is in M-0.1, where $\Delta_{max} = 1.086 \times 10^{-3}\, mm^3$ and 115.2% of V^0_{PVS}.

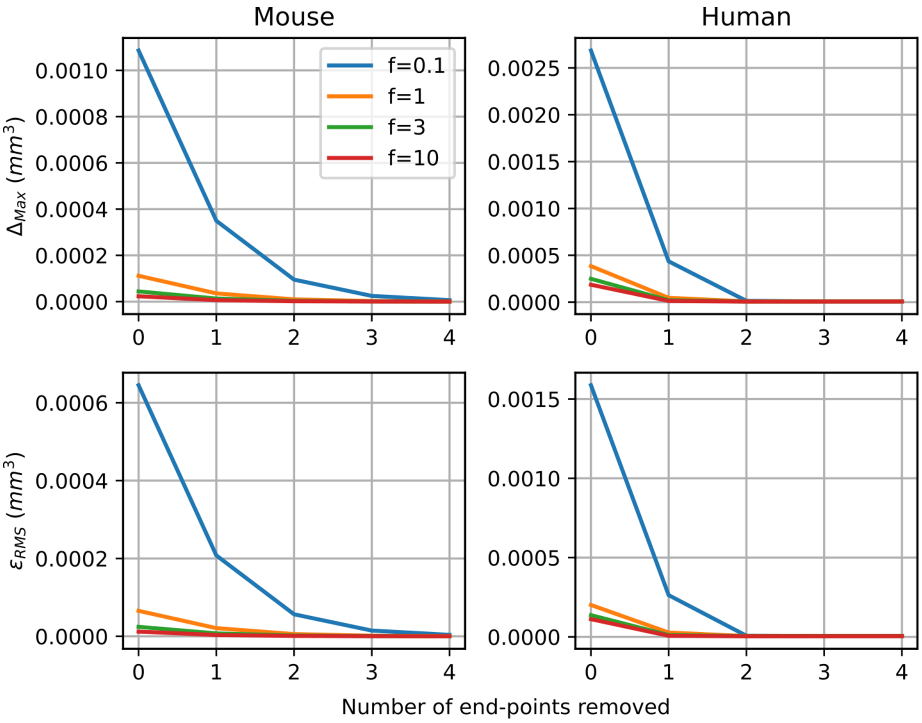

Figure 3.3.1: Max difference and Root Mean Squares difference between PVS volume and total inflow as endpoints are removed.

	i=0	i=1	i=2	i=3	i=4
M-0.1	115.22%	37.10%	10.09%	2.61%	0.67%
H-0.1	2.28%	0.37%	0.01%	<0.01%	<0.01%

Table 3.3.1: Max difference as a percentage of initial domain volume Δ_{max}/V^0_{PVS} for $f = 0.1$ in mouse and human dimensions, at nodes i=[0, 1, 2, 3, 4].

3.4 Outer wall movement

The peak relative outer wall movement was $\left.\frac{R_2}{R_{2,0}}\right._{max} = 1.00624$, and was reached in M-10.

3.5 CFL-number and stability

The tests were run using $cfl = 0.8$ for mouse dimensions and $cfl = 0.9$ for human dimensions. Higher numbers would cause instability.

CHAPTER

FOUR

DISCUSSION

4.1 Choice of model geometry

It is important to note that the geometry chosen in my model is heavily simplified. Penetrating arteriole perivascular spaces are nearly circular, however, the arteriole is located eccentrically to the side, which causes lower resistance to flow [1]. Additionally, there is connective tissue and other non-cellular components present in the PVS. In their 2023 review, Kelley et al.[15] argues for these PVSs to be modeled as a porous media, while in several recent papers it is modeled as an open space governed by Navier Stokes Equations[22][25][12]. Upscaling the mural dimension based on the relative difference in penetrating arteriole radius, was done for simplicity, and although there is shown a correlation between arterial radius and other dimensions like PVS width[26][7], the resulting geometry, may not be fully realistic for a human penetrating arteriole PVS.

1D modeling of the perivascular space has been done before by Daversin-Catty et al. [25]. They also used dimensionally reduced Navier-Stokes equations to describe pulsatile flow resulting from axisymmetric arterial wall movement, and were able to accurately capture the major flow characteristics. Unlike my model, they accounted for the radial velocity u_r at the inner wall, and used a traction condition at the PVS ends. They also modeled the outer wall as rigid, and direct comparison can therefore not be made.

The choice to model the outer wall as thin elastic tissue is also done in Gan et al.[12], and is rooted in Bojarskaite et al.[22] finding considerable changes in the outer wall diameter during the sleep cycle, in their study. These changes are however not likely to be solely due to pressure forces translated through the fluid as in my model as there is found to be threads of connective tissue linking these walls together, that can also be expected to translate forces.

4.2 Model reduction assumptions

Assumption 5 in Section.2.2, dominance of axial velocity does inherently not hold along the walls where the no-slip conditions cause only radial velocity, especially so for the inner wall, which reaches 62.83 $\mu m/s$ in M-10.

As mentioned in Sec.4.1, the central arteriole is in reality placed eccentrically, weakening the validity of the assumption of axial symmetry.
Despite the flow rate deviations at the inlet causing u_{max} to reach over three times the value of any internal point, Re_{max} for the test was 0.2971, in H-10, which is still adequately low to support the use of a Poiseuille flow profile. H-10, representing a 600bpm heart rate in a human-sized system, isn't realistic and Re_{max} is 100 times the maximum Reynold's number of 3×10^{-3} found in [22] and Re 10^{-3} referenced in [15]. $Re_{max} = 0.0306$ for M-10 is only ten times the upper bound used in [22]. They included pial artery PVS, which have higher Reynold's numbers [15], recorded pulsation frequencies up to 15Hz, and used a lower dynamic viscosity of $0.693 \times 10^{-3}\, Pa \cdot s$, as opposed to the 0.9×10^{-3} used in my model. The choice of $\mu = 0.9 \times 10^{-3}$ was made for easier comparison with Gan et al.[12], who used this number in their model.

The pressure gradient for low frequency oscillations was close to constant along the cross-section. This was also the case in [27], however they studied a bifurcated PVS with $P = 0$ at the ends, and modelled the outer wall as rigid. The peak pressure was also only $0.38\, Pa$, with a gradient of $0.84 Pa/mm$. Bojarskaite et al.[22] found a pressure gradient of $11.7\, Pa/mm$ in the case of their non-obstructed PVS, which is close to my value of $12.5\, Pa/mm$ for the mouse trials, however, they also modeled the outer wall as rigid. In the case of 25% and 50% PVS obstruction, their resulting pressure gradients reached $21.3\, Pa/mm$ and $32\, Pa/mm$.

Poiseuille flow profiles in oscillating PVS flow have been observed *in vivo* by Mestre et al.[6], using two-photon microscopy. This was in bifurcated pial artery PVSs, with Reynold's numbers an order of magnitude lower than the lower bound of my trials. The Womersley numbers (Table.3.2.1) being in the order of 10^{-2} does support the choice of flow profile. The choice of $\alpha = 1$ is for the same reason not justified. The simultaneous assumption of Poiseuille flow in the friction term and a flat velocity profile in the momentum flux term has been justified for blood flow at higher Womersley numbers[28][18]. This is likely not transferable to CSF, as it might be attributed to the shear thinning effects of blood, while CSF is Newtonian[15].

4.3 Boundary conditions and inner wall movement

During the characteristic analysis, to arrive at the decoupled equations 2.35, I neglected the friction term, which is likely to have caused problems due to the viscous nature of the flow. This assumption is only made at the boundary nodes, where the deviation in the results are present. Additionally, the inlet boundary condition of constant pressure is in the current model enforced by keeping the outer wall radius constant. This is in conflict with the assumption of constant wall stiffness, and would result in extra terms $\frac{\partial \beta}{\partial z}$ added to the friction term, that are also neglected. The latter only affecting the inlet, where the deviation is considerably larger, strengthens the idea that this assumption is the culprit. This could be investigated by using boundary conditions based on measured pressure and flow data, and implementing them using a method that does not neglect the friction effect.

4.4 Stability

The instability resulting from using CFL-numbers higher than 0.8 for mural and 0.9 for human trials should be noted. The cause of this was not investigated, and is left for further research.

CHAPTER

FIVE

CONCLUSIONS

In this project, I have succeeded in making a 1-dimensional numerical model that simulates flow in the penetrating arteriole PVS of a mouse and human brain, resulting from periodic axisymmetric movement of the vessel wall. For most of the domain, the model generated a periodic, oscillating flow pattern along the PVS, with similar characteristics to those described in the literature. At the boundaries, the results deviated considerably from the internal nodes, resulting in flow rates up to 1.34 times that of any internal nodes for the human dimensions, and up to 3.23 times for the mouse dimensions. The flow in the nodes with deviating results was not physical, as the total flow strongly deviated from the volume change.

The biggest pressure difference from inlet to outlet was 12.5Pa in all trials, giving an average pressure gradient of 12.5Pa/mm in the mouse dimensions and 2.5Pa/mm in the human dimensions. This is in the same order as in other simulations. The Reynold's numbers were approximately 1 to 2 orders of magnitude larger than what's found in simulations of similar systems, even when excluding nodes with unphysical flow results. The peak flow rates were in the upper bound of what's found in other PVS flow simulations. They were expected to be lower, as the elastic outer wall absorbs some pulsation energy where the more commonly used rigid outer wall does not.

I suspect that the unphysical results at the boundaries can be due to the neglecting of friction when deriving the boundary conditions, and the way constant pressure is enforced at the inlet, so future work should examine this by handling the boundary conditions differently.

REFERENCES

[1] Tomas Bohr et al. "The glymphatic system: Current understanding and modeling". In: *iScience* 25.9 (2022), pp. 1–33. ISSN: 25890042. DOI: `10.1016/j.isci.2022.104987`.

[2] Jeffrey J. Iliff et al. "A paravascular pathway facilitates CSF flow through the brain parenchyma and the clearance of interstitial solutes, including amyloid β". In: *Science Translational Medicine* 4.147 (2012), pp. 1–12. ISSN: 19466234. DOI: `10.1126/scitranslmed.3003748`.

[3] Jeffrey J. Iliff et al. "Cerebral arterial pulsation drives paravascular CSF-Interstitial fluid exchange in the murine brain". In: *Journal of Neuroscience* 33.46 (2013), pp. 18190–18199. ISSN: 02706474. DOI: `10.1523/JNEUROSCI.1592-13.2013`.

[4] Jeffrey J. Iliff et al. "Brain-wide pathway for waste clearance captured by contrast-enhanced MRI". In: *Journal of Clinical Investigation* 123.3 (2013), pp. 1299–1309. ISSN: 00219738. DOI: `10.1172/JCI67677`.

[5] Marshall L. Rennels et al. "Evidence for a 'Paravascular' fluid circulation in the mammalian central nervous system, provided by the rapid distribution of tracer protein throughout the brain from the subarachnoid space". In: *Brain Research* 326.1 (1985), pp. 47–63. ISSN: 00068993. DOI: `10.1016/0006-8993(85)91383-6`.

[6] Humberto Mestre et al. "Flow of cerebrospinal fluid is driven by arterial pulsations and is reduced in hypertension". In: *Nature Communications* 9.1 (2018). ISSN: 20411723. DOI: `10.1038/s41467-018-07318-3`. URL: `http://dx.doi.org/10.1038/s41467-018-07318-3`.

[7] Vegard Vinje, Erik N.T.P. Bakker, and Marie E. Rognes. "Brain solute transport is more rapid in periarterial than perivenous spaces". In: *Scientific Reports* 11.1 (2021), pp. 1–11. ISSN: 20452322. DOI: `10.1038/s41598-021-95306-x`. URL: `https://doi.org/10.1038/s41598-021-95306-x`.

[8] Piotr Hadaczek et al. "The "Perivascular Pump" Driven by Arterial Pulsation Is a Powerful Mechanism for the Distribution of Therapeutic Molecules within the Brain". In: *Molecular Therapy* 14.1 (2006), pp. 69–78. ISSN: 15250016. DOI: `10.1016/j.ymthe.2006.02.018`. URL: `http://dx.doi.org/10.1016/j.ymthe.2006.02.018`.

[9] Susanne J. van Veluw et al. “Vasomotion as a Driving Force for Paravascular Clearance in the Awake Mouse Brain”. In: *Neuron* 105.3 (2020), 549–561.e5. ISSN: 10974199. DOI: `10.1016/j.neuron.2019.10.033`. URL: `https://doi.org/10.1016/j.neuron.2019.10.033`.

[10] Ravi Teja Kedarasetti, Patrick J. Drew, and Francesco Costanzo. “Arterial vasodilation drives convective fluid flow in the brain: a poroelastic model”. In: *Fluids and Barriers of the CNS* 19.1 (2022), pp. 1–24. ISSN: 20458118. DOI: `10.1186/s12987-022-00326-y`.

[11] Stephanie Holstein-Rønsbo et al. “Glymphatic influx and clearance are accelerated by neurovascular coupling”. In: *Nature Neuroscience* 26.6 (2023), pp. 1042–1053. ISSN: 15461726. DOI: `10.1038/s41593-023-01327-2`.

[12] Yiming Gan et al. “Perivascular pumping of cerebrospinal fluid in the brain with a valve mechanism”. In: *Journal of the Royal Society Interface* 20.206 (2023). ISSN: 17425662. DOI: `10.1098/rsif.2023.0288`.

[13] Weiwei Jin and Jordi Alastruey. “Arterial pulse wave propagation across stenoses and aneurysms: Assessment of one-dimensional simulations against three-dimensional simulations and in vitro measurements”. In: *Journal of the Royal Society Interface* 18.177 (2021). ISSN: 17425662. DOI: `10.1098/rsif.2020.0881`.

[14] Fatima Min Rivas et al. “Surface periarterial spaces of the mouse brain are open, not porous: Surface periarterial spaces of the mouse brain are open, not porous”. In: *Journal of the Royal Society Interface* 17.172 (2020). ISSN: 17425662. DOI: `10.1098/rsif.2020.0593`.

[15] “Cerebrospinal Fluid Flow”. In: *Annual Review of Fluid Mechanics* 55 (2023), pp. 237–264. ISSN: 00664189. DOI: `10.1146/annurev-fluid-120720-011638`.

[16] Alfio Quarteroni and Luca Formaggia. “Mathematical Modelling and Numerical Simulation of the Cardiovascular System”. In: *Handbook of Numerical Analysis* 12.03 (2004), pp. 3–127. ISSN: 15708659. DOI: `10.1016/S1570-8659(03)12001-7`.

[17] Hellevik, Leif Rune. *Numerical Methods for Engineers.* URL: `https://folk.ntnu.no/leifh/teaching/tkt4140/._main072.html#ch:6_Lax-Wendroff_nonlin`. (accessed: 30.01.2024).

[18] Fredrik Eikeland Fossan. “Comparison of numerical schemes for nonlinear 1-D arterial blood flow modeling Fredrik Eikeland Fossan”. In: June (2015).

[19] Helena E. Schreder et al. “A hydraulic resistance model for interstitial fluid flow in the brain”. In: *Journal of the Royal Society Interface* 19.186 (2022). ISSN: 17425662. DOI: `10.1098/rsif.2021.0812`.

[20] Rune Enger et al. “Dynamics of ionic shifts in cortical spreading depression”. In: *Cerebral Cortex* 25.11 (2015), pp. 4469–4476. ISSN: 14602199. DOI: `10.1093/cercor/bhv054`.

[21] David F. Wilson and Franz M. Matschinsky. “Cerebrovascular Blood Flow Design and Regulation; Vulnerability in Aging Brain”. In: *Frontiers in Physiology* 11.October (2020), pp. 1–16. ISSN: 1664042X. DOI: `10.3389/fphys.2020.584891`.

[22] Laura Bojarskaite et al. "Sleep cycle-dependent vascular dynamics in male mice and the predicted effects on perivascular cerebrospinal fluid flow and solute transport". In: *Nature Communications* 14.1 (2023). DOI: `10.1038/s41467-023-36643-5`.

[23] Francesco Romanò et al. "Peristaltic flow in the glymphatic system". In: *Scientific Reports* 10.1 (2020), pp. 1–17. ISSN: 20452322. DOI: `10.1038/s41598-020-77787-4`. URL: `https://doi.org/10.1038/s41598-020-77787-4`.

[24] Richard Courant. *Methods of mathematical physics : Vol. 2 : Partial differential equations.* New York, 1962.

[25] Cécile Daversin-Catty, Ingeborg G. Gjerde, and Marie E. Rognes. "Geometrically Reduced Modelling of Pulsatile Flow in Perivascular Networks". In: *Frontiers in Physics* 10.May (2022), pp. 1–15. ISSN: 2296424X. DOI: `10.3389/fphy.2022.882260`.

[26] Beatrice Bedussi et al. "Paravascular spaces at the brain surface: Low resistance pathways for cerebrospinal fluid flow". In: *Journal of Cerebral Blood Flow and Metabolism* 38.4 (2018), pp. 719–726. ISSN: 15597016. DOI: `10.1177/0271678X17737984`.

[27] Cecile Daversin-Catty et al. "The mechanisms behind perivascular fluid flow". In: *PLoS ONE* 15.12 December (2020), pp. 1–20. ISSN: 19326203. DOI: `10.1371/journal.pone.0244442`.

[28] N. Stergiopulos, D.F. Young, and T.R. Rogge. "Computer simulation of arterial flow with applications to arterial and aortic stenoses". In: *Journal of Biomechanics* 25.12 (1992). ISSN: 0021-9290. DOI: `https://doi.org/10.1016/0021-9290(92)90060-E`. URL: `https://www.sciencedirect.com/science/article/pii/002192909290060E`.

NTNU

Kunnskap for en bedre verden